nature chemical biology

ARTICLES

https://doi.org/10.1038/s41589-020-0576-z

Designer protein assemblies with tunable phase diagrams in living cells

Meta Heidenreich[1,8], Joseph M. Georgeson[1,8], Emanuele Locatelli[2], Lorenzo Rovigatti[3,4]✉, Saroj Kumar Nandi[5,6], Avital Steinberg[1], Yotam Nadav[1], Eyal Shimoni[7], Samuel A. Safran[5]✉, Jonathan P. K. Doye[3]✉ and Emmanuel D. Levy[1]✉

Protein self-organization is a hallmark of biological systems. Although the physicochemical principles governing protein–protein interactions have long been known, the principles by which such nanoscale interactions generate diverse phenotypes of mesoscale assemblies, including phase-separated compartments, remain challenging to characterize. To illuminate such principles, we create a system of two proteins designed to interact and form mesh-like assemblies. We devise a new strategy to map high-resolution phase diagrams in living cells, which provide self-assembly signatures of this system. The structural modularity of the two protein components allows straightforward modification of their molecular properties, enabling us to characterize how interaction affinity impacts the phase diagram and material state of the assemblies in vivo. The phase diagrams and their dependence on interaction affinity were captured by theory and simulations, including out-of-equilibrium effects seen in growing cells. Finally, we find that cotranslational protein binding suffices to recruit a messenger RNA to the designed micron-scale structures.

The self-organization and proper function of complex systems involve elaborate spatiotemporal coordination of their constituent elements. Cells organize their contents into organelles, which have been classically viewed as membrane-bound structures. However, in recent years an increasing number of studies has described fundamentally different types of organelles that form by phase separation and are not membrane bound[1]. These organelles, also called biomolecular condensates[2], are associated with diverse functions[1,3,4] ranging from pre-messenger RNA processing[5] and translation regulation[6] to signaling[7], or to the formation of eye lenses[8]. The increasingly frequent discovery of such organelles reflects that we are only beginning to grasp the complexity underlying the proteome's spatial organization, and begs for a molecular understanding of the process of phase separation in living cells.

In phase separation, thousands of identical molecules cluster and interact together, implying that small changes in molecular properties of components—for example, by mutation—can propagate and dramatically impact macroscopic phenotypes of assembly[9]. For example, mutations increasing the viscosity of FUS and huntingtin exon 1 condensates have been associated with debilitating diseases such as amyotrophic lateral sclerosis, frontotemporal dementia[10,11] and Huntington's disease[12]. However, there is little understanding of how these mutations act at the molecular level to change the phase behavior and viscosity of condensates. To bridge this gap, it is crucial to connect biophysical properties of proteins to mesoscale phenotypes of their assembly within living cells.

Establishing such a nanoscale–mesoscale connection with natural condensates is hardly possible due to their compositional and regulatory complexity. Creating synthetic condensates offers a powerful alternative, as both the structure and biophysical properties of the components can be known by design. Furthermore, if the proteins employed are orthogonal to the living system, no active cellular regulation is expected to take place. Previous work based on synthetic proteins showed that increasing multivalence of the components promotes their phase separation[13,14], and revealed how distinct client proteins can be differentially recruited to condensates[2]. However, detailed molecular modeling of these systems is difficult since the interaction affinity between individual components was fixed[13] or unknown[14], and the contribution of intra- versus intermolecular interactions was also unknown. Moreover, in such systems, interaction affinities and the balance of inter- versus intramolecular interactions cannot be tuned independently from one another. These limitations prompted us to design a synthetic system providing control over these nanoscale properties.

Here we introduce this minimal system, which consists of two protein components. We show that this system allows the direct visualization of its phase diagram in living cells. By mapping the phase diagram of point mutants modulating the binding affinity between the two components, we demonstrate that increasing affinity enhances phase separation in vivo until the system becomes kinetically trapped at very high affinities. Finally, we applied our system to interrogate biological mechanisms of self-assembly. We found that one of the system's components binds cotranslationally to the condensate, indicating that cotranslational protein binding of a nascent chain can suffice to localize its mRNA.

Results

A synthetic two-protein system that phase separates. A quantitative and detailed molecular understanding of biophysical and biological mechanisms of mesoscale self-assembly requires a system

[1]Department of Structural Biology, Weizmann Institute of Science, Rehovot, Israel. [2]Faculty of Physics, University of Vienna, Vienna, Austria. [3]Physical & Theoretical Chemistry Laboratory, Department of Chemistry, University of Oxford, Oxford, UK. [4]Department of Physics, Sapienza Università di Roma, Rome, Italy. [5]Department of Chemical and Biological Physics, Weizmann Institute of Science, Rehovot, Israel. [6]TIFR Centre for Interdisciplinary Sciences, Tata Institute of Fundamental Research, Hyderabad, India. [7]Department of Chemical Research Support, Weizmann Institute of Science, Rehovot, Israel. [8]These authors contributed equally: Meta Heidenreich, Joseph M. Georgeson. ✉e-mail: lorenzo.rovigatti@uniroma1.it; sam.safran@weizmann.ac.il; jonathan.doye@chem.ox.ac.uk; emmanuel.Levy@weizmann.ac.il

where all parameters, namely the components, their structure and their physical interactions, are known. To this aim, we developed a synthetic system in which these properties are controlled by design. The system comprises two protein components that interact with affinities tunable by point mutation. Each component is designed in a modular fashion and consists of three structured domains linked by short, flexible linkers. As we know from previous work that multivalence is a critical property of molecules undergoing phase separation[13,15], both components are multivalent. The first component contains a homodimerization domain, a red fluorescent protein (RFP) and the protein Im2. The second component contains a homotetramerization domain, a yellow fluorescent protein (YFP) and the protein E9, which interacts specifically with Im2 (Fig. 1a and Supplementary Table 1; Methods). Importantly, unlike in other synthetic systems[13,14], intramolecular interactions are restricted by an incompatibility between the distances separating the termini to which interaction domains are fused, equal to 18 nm on the dimer and only 4 nm on the tetramer (Fig. 1a,b).

We coexpressed the dimer and tetramer components in yeast cells. Using fluorescence microscopy, we observed the formation of submicron- to micron-scale punctate assemblies where the tetramer and dimer colocalized (Fig. 1c and Supplementary Video 1), suggesting that the system undergoes phase separation and forms condensates. The assembly of this system was dependent on the specific interaction between E9 and Im2, as condensates were observed neither when coexpressing the tetramer with a dimer lacking the Im2 domain (Fig. 1d), nor in haploid cells expressing only one of the components (Extended Data Fig. 1). The assemblies were not membrane bound as visualized by electron microscopy (Extended Data Fig. 2).

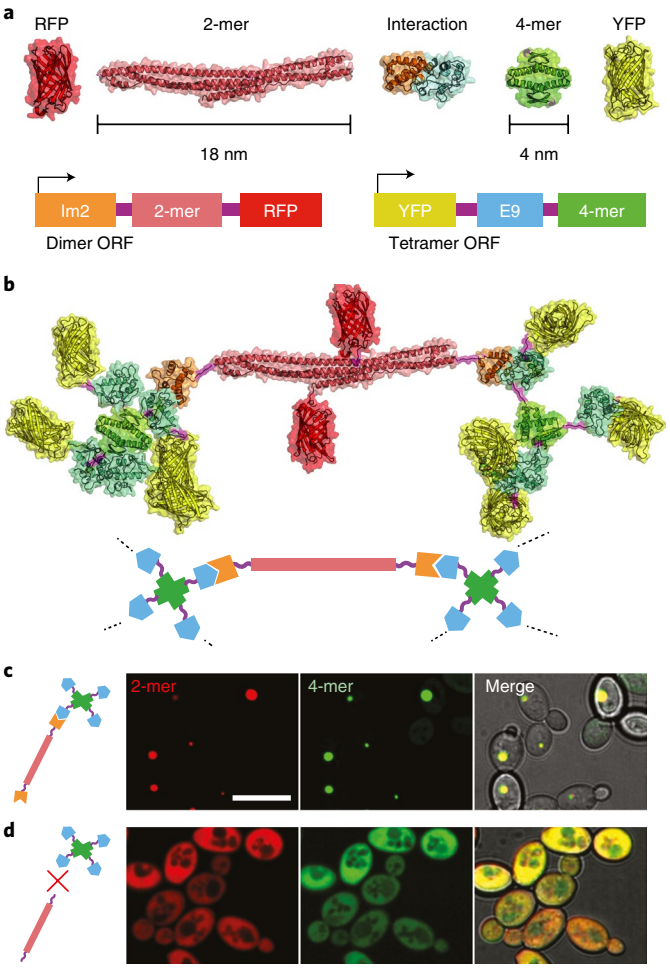

Fig. 1 | A synthetic system for controlled phase separation in living cells. **a**, The components, each encoded in one ORF, consist of three domains connected by flexible linkers: an interaction domain, an oligomerization domain and a fluorescent protein. The colicin (E9, cyan) and immunity (Im2, orange) proteins serve as interaction modules where affinity is controllable by mutation. A dimer and tetramer of known structure (Supplementary Table 1) served as divalent and tetravalent scaffolds, respectively. We fused Im2 and a RFP to the dimer, and E9 and a YFP to the tetrameric scaffold. **b**, Illustrative structure of a dimer interacting with two tetramers, and a cartoon representation below. **c**, The system undergoes self-assembly and forms punctate structures in living yeast cells. Scale bar, 10 µm. **d**, In the absence of the Im2 interaction module, no punctate structure is formed. These results were independently replicated three times.

Revealing phase diagrams in vivo at high resolution. The physical origin of phase separation of molecules in solution is the attraction between them, which, in the appropriate ranges of concentration and interaction strength, dominates the entropy of mixing. In our system, dimers mediate indirect tetramer–tetramer attraction. At equilibrium, this attraction gives rise to two coexisting phases with equal chemical potential and osmotic pressure: a dense phase where tetramers and dimers show high concentrations, high enthalpy and low entropy, and a dilute phase with lower concentrations of dimers and tetramers, lower enthalpy and higher entropy.

In cells, the dense phase corresponds to the condensate and the dilute phase consists of components freely diffusing within the cytoplasm (Fig. 2a). The conditions under which phase separation occurs at equilibrium are described by its phase diagram, with the binodal defining phase boundaries. We developed a lattice model (Fig. 2b; Methods) to predict the phase diagram of our system as a function of dimer and tetramer concentrations (Fig. 2c). Concentrations outside of the binodal do not drive phase separation, either because they are too low relative to the interaction affinity (Fig. 2d) or because an imbalance in the components' stoichiometry inhibits the propagation of their interactions in multicomponent systems[13,15–20] (Fig. 2e).

Interestingly, because cells without condensates have not undergone phase separation and should fall outside of the binodal, the region of concentrations that is absent in these cells should reveal the phase boundary of this system (Fig. 2f). Such an approach offers the unique opportunity to map a high-resolution phase diagram in vivo, because the phase space can be defined along two continuous coordinates corresponding to the concentrations of each component. Unlike temperature or pressure, protein concentration can be tuned over several orders of magnitude and may be measured readily from fluorescence intensity across thousands of single cells.

To characterize such a phase diagram, we created yeast strains coexpressing the dimer and tetramer components independently, such that each cell sampled a different point of the phase space. We imaged thousands of single cells and estimated components' concentrations from fluorescence intensity (Supplementary Fig. 1), excluding cells containing a condensate, to ascertain reliable concentration measurements (Fig. 2f; Methods). As predicted, the density distribution of cells revealed the phase boundary of the system (Fig. 2g).

Modeling the phase diagram measured in vivo. The phase boundary appears as an area where cell density approaches zero. The scarcity of cell sampling concentrations beyond 10 µM prevented visualizion of closed boundaries, giving rise to a half-ellipsoid. We modeled the expected boundaries using a minimal lattice model where tetramers occupy the vertices, dimers occupy the bonds and solvent molecules can occupy either vertices or bonds. (Fig. 2b,c; Methods).

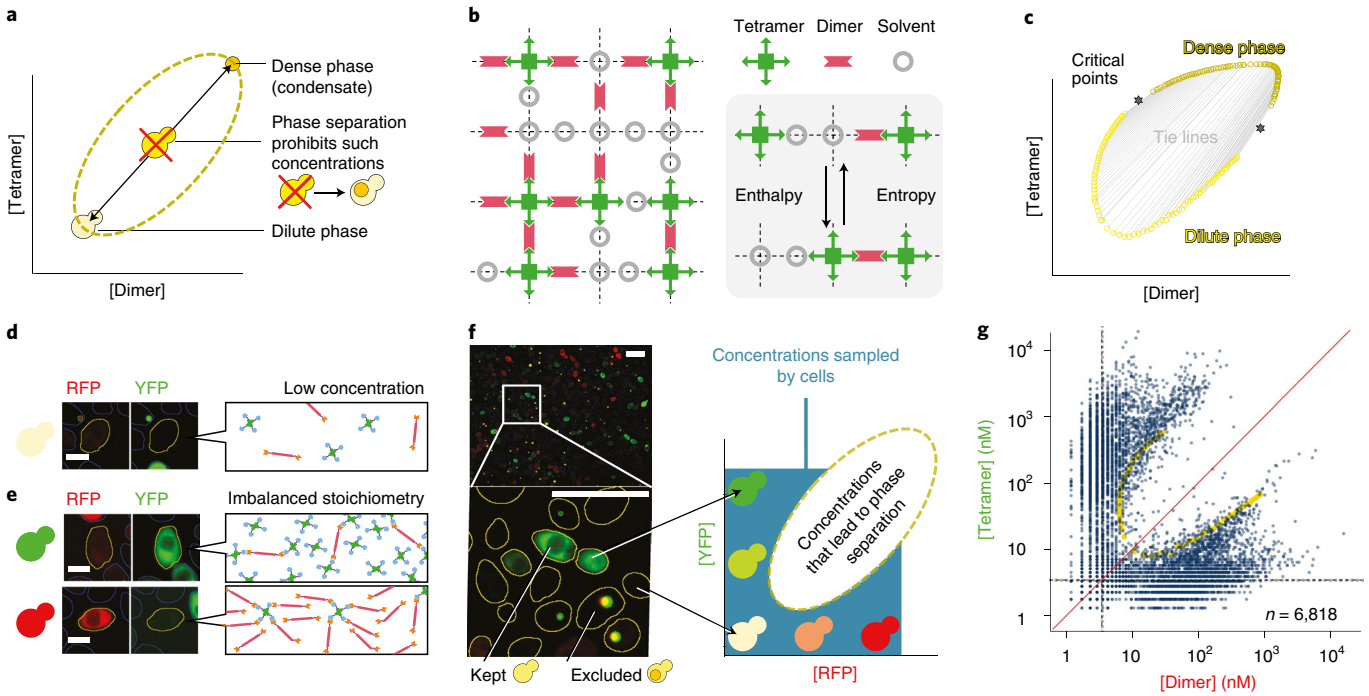

Fig. 2 | Characterization of phase diagrams in living cells. a, The phase diagram describes when the system phase separates in a given parameter space, here defined by dimer and tetramer concentrations. Concentrations within the binodal (yellow dashed line) are not stable, as for the crossed-out cell, leading to phase separation into dilute and dense phases (condensate). **b**, A lattice model captures the essence of phase separation whereby the chemical potential of the dimer and tetramer exhibit two minima, the first with high entropy and low enthalpy (dilute phase) and the second with low entropy and high enthalpy from the bonding energy (dense phase). **c**, Based on this lattice model we derive a phase diagram showing the binodal, two critical points and tie lines. **d**, Cells without condensate may have concentrations of both components that are too low. **e**, Alternatively, cells without condensate may exhibit an imbalanced stoichiometry where binding sites of the component of lower concentration are saturated with the component in excess. **f**, Cells are imaged and segmented, and those with condensates are excluded. The concentrations of dimer (RFP, red), and tetramer (YFP, green) binding sites are recorded and plotted against each other. Both components are coexpressed stochastically, so each cell samples one point of the phase diagram. Scale bars, 10 µm. **g**, In vivo phase diagram of our synthetic system containing wild-type Im2 and E9 interacting with a reported affinity of 15 nM (Table 1). Each point represents a single cell ($n = 6{,}818$) and shows binding site concentrations of the dimer (x axis) and tetramer (y axis). The red line highlights the diagonal. Gray dashed lines delimit background fluorescence levels below which concentrations cannot be estimated reliably (~3.5 nM). The yellow points show an overlay of the computed binodal based on the lattice model (Methods). The striped pattern visible at low concentrations along both axes results from the use of median intensity values, which are discrete numbers.

Table 1 | Im2 variants previously reported and used to modulate dimer–tetramer interaction affinity

Im2 mutation	K_d with E9 (M)
D33L N34V R38T[a]	$3.4 \pm 1.4 \times 10^{-13}$
D33L	$4.8 \pm 0.3 \times 10^{-11}$
N34V R38T[a]	$1.9 \pm 0.4 \times 10^{-10}$
R38T[a]	$2.6 \pm 0.5 \times 10^{-9}$
N34V[a]	$3.3 \pm 0.7 \times 10^{-9}$
WT	$1.5 \pm 0.1 \times 10^{-8}$
E30A	$2.8 \pm 1.6 \times 10^{-7}$
P56A	$2.1 \pm 0.7 \times 10^{-6}$
V37A	$9.3 \pm 4.4 \times 10^{-6}$

Previously reported[21] mean and s.e.m. values of the affinities are given ($n = 2$). [a]Mutants added later in this work, for which we derived phase diagrams only.

Furthermore, we generated phase diagrams using a thermodynamic perturbation theory developed for patchy particles matching the geometry of our proteins (Supplementary Fig. 2; Supplementary Note). Both methodological approaches recapitulated our observations: the half-ellipsoid aligns along the diagonal where the stoichiometry of both components' binding sites is equal (Fig. 2g and Extended Data Fig. 3). Indeed, a balanced stoichiometry gives rise to a lower energy assembly where enthalpy is maximal with all binding sites satisfied, thus favoring phase separation. As stoichiometries become unbalanced (for example, 1:10 or 10:1), the component present in excess saturates all binding sites of its partner, which inhibits propagation of interactions and phase separation (Fig. 2e).

Tuning phase diagram and viscosity by affinity. The nature of the interaction domains used in this system allows both lowering and increasing the affinity by single point mutations[21] described in Table 1. We initially investigated four new variants for the dimer, which contained point mutations modulating the dissociation constant (K_d) between domains Im2 and E9 across five orders of magnitude, from 10^{-11} to 10^{-6} M.

We imaged yeast cells coexpressing the tetramer with the new dimer variants, and generated their in vivo phase diagrams (Fig. 3 and Extended Data Fig. 5). Mutants interacting with an affinity lower than that of the wild-type domains showed a shift in their phase diagram. The half-ellipsoid underwent a translation along the diagonal, towards higher concentrations. Such a translation was expected, as lower interaction affinities require higher concentrations for binding. The same effect was reproduced with the two theoretical approaches we put forward (Extended Data Fig. 3). Interestingly, the mutant with an affinity of 4.8×10^{-11} M (higher affinity than the

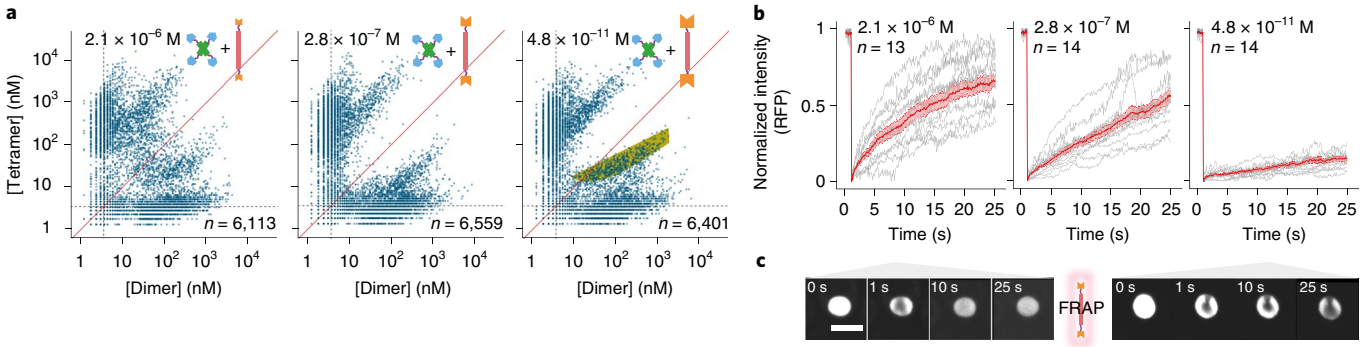

Fig. 3 | Influence of affinity on phase separation in vivo. a, Phase diagrams of the tetramer with the dimer carrying three different affinities, as indicated. The red line highlights the diagonal. The gray dashed lines indicate the fluorescence accuracy limit (~3.5 nM) below which autofluorescence increases. The yellow band highlights a region where phase separation occurs with wild-type Im2, but does not occur with the high-affinity mutant. **b**, FRAP experiments were carried out for three pairs of components varying in their interaction affinity. Increasing interaction affinity increased the effective viscosity of the condensate. Gray lines show individual repeats, the red line indicates the mean and red area shows s.e.m. Sample sizes are indicated in each plot. **c**, Example of two condensates recovering after photobleaching. Low-affinity interaction (left) shows faster recovery when compared with condensates involving higher affinities (right). Scale bar, 5 μm.

wild type) revealed a complex behavior: the minimal concentration of tetramer required for phase separation increased, as reflected in the upward shift of the phase boundary (yellow region, Fig. 3a).

This upward shift led us to examine the diffusion dynamics of components within condensates. Fast diffusion requires components to be unbound, and their probability of existing in the unbound state is inversely proportional to their interaction affinity (Supplementary Note). Thus, we expect high-affinity interactions to yield condensates with slow diffusion dynamics whereas lower affinities should yield faster diffusion dynamics. To test this hypothesis, we measured fluorescence recovery after photobleaching (FRAP) of condensates. Considering low-, medium- and high-affinity interactions (2.1×10^{-6}, 2.8×10^{-7} and 4.8×10^{-11} M, respectively), mean fluorescence recovery after 25 s reached $65\pm4\%$, $56\pm4\%$ and $15\pm2\%$, respectively (Fig. 3b,c, Extended Data Fig. 5 and Supplementary Video 2). Individual traces show pronounced variability in the recovery profile, especially at low affinities, which might reflect differences in both condensate density and the fraction of bonded components (Supplementary Fig. 3). On average, however, higher interaction affinity led to slower diffusion of components, consistent with the effective viscosity of the condensates being controlled by interaction affinity. Importantly, the slower recovery of the D33L Im2 mutant implies that it does interact with a higher affinity than wild-type Im2, which is in conflict with the observed shrinkage in phase boundaries (yellow region, Fig. 3a). This apparent contradiction may originate in kinetics. At high affinity, the kinetics of unbinding events is very slow, which can trap the system in states where both components have a nonoptimal distribution of bonds in the network. Nonetheless, dimers need to be completely bonded to mediate cluster growth whereas tetramers require only two out of four bonds to mediate such growth. Consequently, misplaced bonds in a tetramer-poor system would hinder the formation of a network more than they would in a tetramer-rich system. This idea led us to compare the regions where phase separation occurs in equilibrium versus out-of-equilibrium molecular dynamics simulations of patchy particles (Extended Data Fig. 4a). These simulations confirmed the picture sketched above, by revealing a shift in the lower branch of the phase diagram while the upper branch remained essentially unmoved (Extended Data Fig. 4b, Supplementary Figs. 4 and 5 and Supplementary Note).

To further corroborate that kinetic trapping inhibits phase separation, we created a yeast strain where components interact with an even higher affinity (3.4×10^{-13} M; Table 1). This mutant showed a more pronounced upward shift of the lower branch, further supporting that the system becomes kinetically trapped at very high affinities (Extended Data Fig. 6). Moreover, to narrow the affinity range at which kinetic trapping becomes visible, we created three additional variations of the system where the dimer and tetramer interact with intermediate affinity (3.3×10^{-9}, 2.6×10^{-9} and 1.9×10^{-10} M; Table 1). We measured in vivo phase diagrams for these new variants and observed that the upward shift appears at an affinity of 1.9×10^{-10} M and becomes pronounced only at 4.8×10^{-11} M (Extended Data Fig. 6).

Cotranslational binding suffices to localize mRNA. The spatial organization of translation is achieved by mRNA trafficking and localization[22]. Interestingly, mRNA localization could be achieved by protein synthesis if they can bind localized partners cotranslationally. This mechanism had, in fact, been suggested to mediate the localization of mRNAs encoding myosin heavy chain in developing cultured skeletal muscles[23]. However, when considering a biological system, it is hard to address whether cotranslational binding of a nascent polypeptide chain can suffice to localize its encoding mRNA, because other mechanisms may be involved.

Additionally, cotranslational binding can be hindered by numerous factors. Indeed, polysomes diffuse more slowly than globular proteins due to their large size, so a nascent chain may not reach a particular localization within the time of translation. In parallel, the interacting region of the nascent chain must be exposed at the surface of the ribosome for a sufficiently long time to mediate binding with the target. As a result, and as observed for cotranslational assembly of protein complexes[24–26], the N- versus C-terminal positioning of the interaction region may play an important role. These limiting factors beg the question: can cotranslational binding suffice to determine the localization of a polysome?

Uniquely, our synthetic system makes it possible to address this question directly because we know that its components have evolved neither to bind their own mRNA, nor RNAs in general. We fused the mRNA encoding the dimer component to a sequence enabling its tracking in live cells[27]. In these experiments we used a tetramer component fused to a blue fluorescent reporter, so that green fluorescence was reporting solely on mRNA localization. Live cell imaging revealed that mRNAs diffused throughout the cell and attached to the condensate when they encountered it. Surprisingly, multiple mRNAs could colocalize and appeared to nucleate the formation of the condensate (Fig. 4a,d and Supplementary Video 3). In contrast,

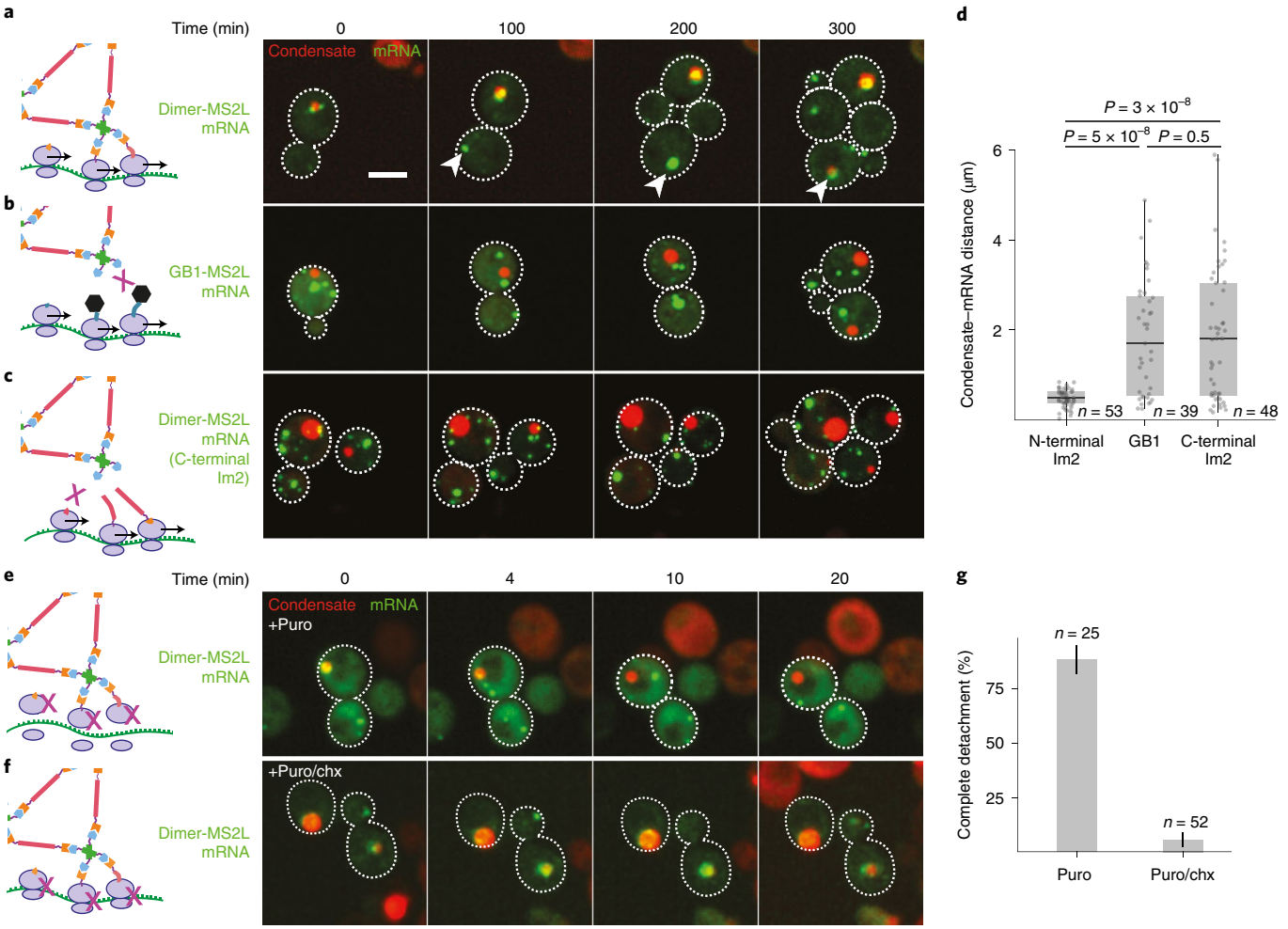

Fig. 4 | Cotranslational binding of a nascent chain directs mRNA localization. a, The mRNA of the dimeric component was tagged with the MS2L sequence, and appears in live cells as green fluorescent puncta[27]. The tetrameric component did not contain YFP, so the condensates are shown with red fluorescence only. mRNA molecules encoding for the dimer colocalize with the condensate. Arrowheads highlight an mRNA cluster that appears before the condensate. Scale bar, 5 μm. **b**, mRNAs of a control protein (GB1) do not colocalize with condensates. **c**, When the binding domain Im2 is encoded at the C terminus of the dimer, the mRNA does not colocalize with the condensate. **d**, Quantification of experiments depicted in **a**–**c**, Cells were automatically segmented from brightfield microscopy images. When foci were detected in both (red and green) channels, their distance was calculated from the coordinates of the brightest detected foci in the maximum z-projection of seven stacks. Boxes delineate the first and third quartiles, the black line corresponds to the median while upper and lower whiskers extend to the highest and lowest values and, at most, 1.5 times the interquartile range. *P* values are indicated above (one-sided *t*-test). **e**, Puromycin (puro.) treatment dissociates ribosomes from mRNA and releases dimer mRNA from the condensate. **f**, Puromycin-induced dissociation of mRNA does not occur when cycloheximide (chx), a drug that inhibits puromycin-dependent runoff of polysomes, is coadministered with puromycin. **g**, Quantification of experiments depicted in **d**,**e**, Cells exhibiting colocalization of mRNA and condensate were followed after treatment with either puromycin per se or coadministered with cycloheximide for 25 min. The fraction of cells exhibiting complete detachment of mRNA punctae from condensates is shown. Error bars represent 1 s.d.

an mRNA coding for a protein that does not bind to the condensate did not colocalize with it (Fig. 4b,d and Supplementary Video 4). As an additional control, we changed the position of the binding domain of the dimer from the N to the C terminus. In this new construct, the binding domain is released from the ribosome immediately after its synthesis. Therefore, this construct is not expected to mediate cotranslational assembly[24,25] and its mRNA should not localize to the condensate. In agreement with this prediction, we did not observe recruitment of dimer mRNA to the condensate when the binding domain was encoded in its C terminus (Fig. 4c,d and Supplementary Video 5). This result also implies that dimerization does not occur cotranslationally, possibly because the dimer interface involves the C terminus that is not exposed at the surface of the ribosome for a sufficiently long time.

To provide a quantitative description of these live cell-imaging observations, we measured the distribution of distances between the center of foci corresponding to mRNAs (green) and condensates (red; see Methods). As expected, the mRNAs of dimers harboring an N-terminal binding region colocalized with condensates (mean distance, 0.48 ± 0.19 μm), whereas the mRNAs of dimers harboring a C-terminal binding domain showed a mean distance of 1.85 ± 1.49 μm and encompassed values as large as the diameter of a yeast cell. This latter distance distribution is not significantly different from that of a negative control—that is, a mRNA encoding a protein that does not bind to the condensate (mean distance, 1.83 ± 1.29 μm).

To ascertain that recruitment of mRNA to the condensate is translation dependent we employed puromycin, a drug that

dissociates translating ribosomes from mRNA. Treatment of cells with puromycin released dimer mRNA from the condensate within minutes (Fig. 4e, Supplementary Video 6 and Extended Data Fig. 7). Interestingly, cycloheximide prevents puromycin-mediated dissociation of ribosomes from their mRNA[28], providing another means to test the translation dependence of mRNA localization on the condensate. When treated simultaneously with puromycin and cycloheximide, mRNAs maintained their colocalization with condensates (Fig. 4f and Supplementary Video 7).

To gain a quantitative view of these experiments, we followed cells exhibiting colocalization between mRNA and condensate before treatment and recorded how many of these exhibited complete detachment of mRNA after treatment with puromycin alone, or puromycin together with cycloheximide (Extended Data Fig. 7; Fig. 4g). While puromycin treatment led to complete detachment of mRNA(s) in 88% of cases, the addition of cycloheximide canceled this effect as complete detachment occurred in only 6% of cases (Fig. 4g). Together, these results point to cotranslational binding of a nascent chain as a mechanism that can drive the localization of its encoding mRNA.

Discussion and conclusions

We designed and characterized a synthetic minimal system to study in vivo phase separation from first principles. Notably, the folded nature of interaction domains of our system, together with the defined geometry of oligomerization domains, provide unprecedented control over the biophysical and structural properties of the components. At the same time we introduce a new strategy using single cells as individual 'test tubes' to map high-resolution phase diagrams in vivo. Combined, these properties create a powerful experimental system to relate nanoscale to mesoscale phenotypes of self-assembly from first principles. We explore this relationship by characterizing how mutations changing the interaction affinity between the two components impact the phase behavior and material state of the condensates they form. Interestingly, numerous additional parameters such as linker properties, electrostatics or valence could be tuned independently from one another, and their impact on phase separation characterized and modeled in the same way.

The ability to dissect how individual parameters impact phase separation is essential for understanding biological condensates, because they involve several layers of complexity. At a biophysical level, intricate dependencies can exist between three parameters: affinity, multivalence and concentration. For instance, an increased valence will lead to an increased apparent affinity which, in turn, lowers the minimal concentration for phase separation[13,29]. At the same time, the apparent valence of a molecule with multiple self-interacting regions can change with concentration if inter- and intramolecular binding events compete[30–32]. Furthermore, at a biological level, the identity of the components, the way in which they interact and how they are regulated are often unknown.

Our system helps address these layers of complexity: biophysically, the impact of intermolecular interaction affinity we observed is also expected in biological systems. For example, increased salt concentration inhibits phase separation and decreases the viscosity of LAF-1 condensates[33]. These results are consistent with our observations, whereby salt would decrease the effective affinity of LAF-1 for itself. Conversely, mutations in the low-complexity domain of TIA1 were shown to enhance its phase separation and decrease its mobility in condensates[34]. In line with our results, these observations indicate a strengthening of intermolecular interactions in TIA1 condensates. At a biological level, the oval-shaped phase boundaries imply that increasing the expression of components in vivo can inform as to whether single or multiple components are required for phase separation. Indeed, in a multicomponent system, increasing the concentration of one component relative to the other dissolves the dense phase at equilibrium. However, if a single component is sufficient, increasing its concentration will result in a larger dense phase. Theoretically, this prediction applies to condensates involving any type of molecule (e.g., folded proteins, disordered regions, RNAs or a combination of these). For example, NPM1 and poly(PR) peptides interact and phase separate together. Similar to our system, very high concentrations of poly(PR) lead to droplet dissolution in vitro[35]. Such behavior has also been described for a system involving RNA interacting with PR-rich peptides[36].

Finally, our synthetic system can serve to identify new synergisms between protein self-assembly and cellular processes. Recent works have revealed cotranslational assembly of complexes as a widespread mechanism[24,37] actively shaped by evolution[25,38]. Our results now suggest that cotranslational binding of a nascent chain can be sufficient to localize mRNAs in cells. Interestingly, several mechanisms for mediating interactions between RNA and proteins in condensates are known[39,40], and the results presented here suggest cotranslational assembly as a new mechanism of this type. The design of mesoscale synthetic protein assemblies is becoming increasingly powerful to create new materials[41–43] and functions[44,45]. Moreover, as we are only beginning to grasp the complexity of proteome self-organization, new approaches are needed for characterizing and understanding mesoscale properties of protein self-assembly in cells[19,20,32,46–51]. In this context, our synthetic system constitutes a powerful tool to interrogate biological mechanisms of protein assembly. In the future, it may serve to evaluate and calibrate physical models of self-assembly in vivo, and form a basis for developing new biomaterials and scaffolds in living cells.

Online content

Any Nature Research reporting summaries, source data, extended data, supplementary information, acknowledgements, peer review information; details of author contributions and competing interests; and statements of data and code availability are available at https://doi.org/10.1038/s41589-020-0576-z.

Received: 6 August 2019; Accepted: 22 May 2020;
Published online: 13 July 2020

References

1. Hyman, A. A., Weber, C. A. & Julicher, F. Liquid–liquid phase separation in biology. *Annu. Rev. Cell Dev. Biol.* **30**, 39–58 (2014).
2. Banani, S. F. et al. Compositional control of phase-separated cellular bodies. *Cell* **166**, 651–663 (2016).
3. Holehouse, A. S. & Pappu, R. V. Functional implications of intracellular phase transitions. *Biochemistry* **57**, 2415–2423 (2018).
4. Banani, S. F., Lee, H. O., Hyman, A. A. & Rosen, M. K. Biomolecular condensates: organizers of cellular biochemistry. *Nat. Rev. Mol. Cell Biol.* **18**, 285–298 (2017).
5. Tatomer, D. C. et al. Concentrating pre-mRNA processing factors in the histone locus body facilitates efficient histone mRNA biogenesis. *J. Cell Biol.* **213**, 557–570 (2016).
6. Buchan, J. R. & Parker, R. Eukaryotic stress granules: the ins and outs of translation. *Mol. Cell* **36**, 932–941 (2009).
7. Su, X. et al. Phase separation of signaling molecules promotes T cell receptor signal transduction. *Science* **352**, 595–599 (2016).
8. Cai, J., Townsend, J. P., Dodson, T. C., Heiney, P. A. & Sweeney, A. M. Eye patches: protein assembly of index-gradient squid lenses. *Science* **357**, 564–569 (2017).
9. Garcia-Seisdedos, H., Empereur-Mot, C., Elad, N. & Levy, E. D. Proteins evolve on the edge of supramolecular self-assembly. *Nature* **548**, 244–247 (2017).
10. Murakami, T. et al. ALS/FTD mutation-induced phase transition of FUS liquid droplets and reversible hydrogels into irreversible hydrogels impairs RNP granule function. *Neuron* **88**, 678–690 (2015).
11. Patel, A. et al. A liquid-to-solid phase transition of the ALS protein FUS accelerated by disease mutation. *Cell* **162**, 1066–1077 (2015).
12. Peskett, T. R. et al. A liquid to solid phase transition underlying pathological huntingtin exon1 aggregation. *Mol. Cell* **70**, 588–601 (2018).
13. Li, P. et al. Phase transitions in the assembly of multivalent signalling proteins. *Nature* **483**, 336–340 (2012).
14. Bracha, D. et al. Mapping local and global liquid phase behavior in living cells using photo-oligomerizable seeds. *Cell* **175**, 1467–1480 (2018).

15. Flory, P. J. *Principles of Polymer Chemistry* (Cornell Univ. Press, 1953).
16. Smallenburg, F., Leibler, L. & Sciortino, F. Patchy particle model for vitrimers. *Phys. Rev. Lett.* **111**, 188002 (2013).
17. Bianchi, E., Largo, J., Tartaglia, P., Zaccarelli, E. & Sciortino, F. Phase diagram of patchy colloids: towards empty liquids. *Phys. Rev. Lett.* **97**, 168301 (2006).
18. Falkenberg, C. V., Blinov, M. L. & Loew, L. M. Pleomorphic ensembles: formation of large clusters composed of weakly interacting multivalent molecules. *Biophys. J.* **105**, 2451–2460 (2013).
19. Jacobs, W. M. & Frenkel, D. Phase transitions in biological systems with many components. *Biophys. J.* **112**, 683–691 (2017).
20. Sanders, D. W. et al. Competing protein-RNA interaction networks control multiphase intracellular organization. *Cell* **181**, 306–324 (2020).
21. Li, W. et al. Dual recognition and the role of specificity-determining residues in colicin E9 DNase–immunity protein interactions. *Biochemistry* **37**, 11771–11779 (1998).
22. Buxbaum, A. R., Haimovich, G. & Singer, R. H. In the right place at the right time: visualizing and understanding mRNA localization. *Nat. Rev. Mol. Cell Biol.* **16**, 95–109 (2015).
23. Isaacs, W. B. & Fulton, A. B. Cotranslational assembly of myosin heavy chain in developing cultured skeletal muscle. *Proc. Natl Acad. Sci. USA* **84**, 6174–6178 (1987).
24. Shiber, A. et al. Cotranslational assembly of protein complexes in eukaryotes revealed by ribosome profiling. *Nature* **561**, 268–272 (2018).
25. Natan, E. et al. Cotranslational protein assembly imposes evolutionary constraints on homomeric proteins. *Nat. Struct. Mol. Biol.* **25**, 279–288 (2018).
26. Kramer, G., Shiber, A. & Bukau, B. Mechanisms of cotranslational maturation of newly synthesized proteins. *Annu. Rev. Biochem.* **88**, 337–364 (2019).
27. Haim-Vilmovsky, L. & Gerst, J. E. m-TAG: a PCR-based genomic integration method to visualize the localization of specific endogenous mRNAs in vivo in yeast. *Nat. Protoc.* **4**, 1274–1284 (2009).
28. Lui, J. et al. Granules harboring translationally active mRNAs provide a platform for P-body formation following stress. *Cell Rep.* **9**, 944–954 (2014).
29. Shin, Y. et al. Spatiotemporal control of intracellular phase transitions using light-activated optoDroplets. *Cell* **168**, 159–171 (2017).
30. Dignon, G. L., Zheng, W., Best, R. B., Kim, Y. C. & Mittal, J. Relation between single-molecule properties and phase behavior of intrinsically disordered proteins. *Proc. Natl Acad. Sci. USA* **115**, 9929–9934 (2018).
31. Dignon, G. L., Zheng, W. & Mittal, J. Simulation methods for liquid–liquid phase separation of disordered proteins. *Curr. Opin. Chem. Eng.* **23**, 92–98 (2019).
32. Yang, P. et al. G3BP1 Is a tunable switch that triggers phase separation to assemble stress granules. *Cell* **181**, 325–345 (2020).
33. Elbaum-Garfinkle, S. et al. The disordered P granule protein LAF-1 drives phase separation into droplets with tunable viscosity and dynamics. *PNAS* **112**, 7189–7194 (2015).
34. Mackenzie, I. R. et al. TIA1 mutations in amyotrophic lateral sclerosis and frontotemporal dementia promote phase separation and alter stress granule dynamics. *Neuron* **95**, 808–816 (2017).
35. White, M. R. et al. C9orf72 Poly(PR) dipeptide repeats disturb biomolecular phase separation and disrupt nucleolar function. *Mol. Cell* **74**, 713–728 (2019).
36. Banerjee, P. R., Milin, A. N., Moosa, M. M., Onuchic, P. L. & Deniz, A. A. Reentrant phase transition drives dynamic substructure formation in ribonucleoprotein droplets. *Angew. Chem. Int. Ed. Engl.* **56**, 11354–11359 (2017).
37. Duncan, C. D. S. & Mata, J. Widespread cotranslational formation of protein complexes. *PLoS Genet.* **7**, e1002398 (2011).
38. Shieh, Y.-W. et al. Operon structure and cotranslational subunit association direct protein assembly in bacteria. *Science* **350**, 678–680 (2015).
39. Langdon, E. M. & Gladfelter, A. S. A new lens for RNA localization: liquid–liquid phase separation. *Annu. Rev. Microbiol.* **72**, 255–271 (2018).
40. Boeynaems, S. et al. Protein phase separation: a new phase in cell biology. *Trends Cell Biol.* **28**, 420–435 (2018).
41. Garcia-Seisdedos, H., Villegas, J. A. & Levy, E. D. Infinite assembly of folded proteins in evolution, disease, and engineering. *Angew. Chem. Int. Ed. Engl.* **58**, 5514–5531 (2019).
42. Shen, H. et al. De novo design of self-assembling helical protein filaments. *Science* **362**, 705–709 (2018).
43. Abe, S. et al. Crystal engineering of self-assembled porous protein materials in living cells. *ACS Nano* **11**, 2410–2419 (2017).
44. Reinkemeier, C. D., Girona, G. E. & Lemke, E. A. Designer membraneless organelles enable codon reassignment of selected mRNAs in eukaryotes. *Science* **363**, eaaw2644 (2019).
45. Lee, M. J. et al. Engineered synthetic scaffolds for organizing proteins within the bacterial cytoplasm. *Nat. Chem. Biol.* **14**, 142–147 (2018).
46. Delarue, M. et al. mTORC1 controls phase separation and the biophysical properties of the cytoplasm by tuning crowding. *Cell* **174**, 338–349. (2018).
47. Chavent, M. et al. How nanoscale protein interactions determine the mesoscale dynamic organisation of bacterial outer membrane proteins. *Nat. Commun.* **9**, 2846 (2018).
48. Alberti, S., Gladfelter, A. & Mittag, T. Considerations and challenges in studying liquid–liquid phase separation and biomolecular condensates. *Cell* **176**, 419–434 (2019).
49. Wang, J. et al. A molecular grammar governing the driving forces for phase separation of prion-like RNA binding proteins. *Cell* **174**, 688–699 (2018).
50. Choi, J.-M., Dar, F. & Pappu, R. V. LASSI: a lattice model for simulating phase transitions of multivalent proteins. *PLoS Comput. Biol.* **15**, e1007028 (2019).
51. Panasenko, O. O. et al. Co-translational assembly of proteasome subunits in NOT1-containing assemblysomes. *Nat. Struct. Mol. Biol.* **26**, 110–120 (2019).

Methods

Design. The synthetic system introduced in this work relies on homo-oligomerization to create multivalent components. We chose particular homo-oligomerization domains to avoid intramolecular interactions between components. Specifically, we selected a large dimer and a small tetramerization domain such that the dimers could bridge across two tetramers but could not bind two sites on the same tetramer. The dimer consists of an antiparallel coiled coil in which both N termini are 18 nm apart. The tetramer is comparatively small and corresponds to the tetramerization domain of p53 (details of protein structures and references appear in Supplementary Table 1).

To avoid nonspecific interactions of the dimer protein, we mutated highly exposed and hydrophobic surface residues to charged ones (Y22D, I92D). For the tetrameric component, we used the wild-type sequence of the tetramerization domain of human p53 from amino acids 326–356. The yellow fluorescent reporter was fused to the tetramer and the red fluorescent protein to the dimer (details of fluorescent proteins and references can be found in Supplementary Table 1). Both fluorescent proteins used are monomeric to prohibit unspecific interactions between the components. Interaction domains were derived from the bacterial toxin–antitoxin system E9/Im2. Different affinities were achieved by introducing point mutations in the sequence of Im2 (Table 1). An H103A mutant of E9 was used to inhibit its toxic DNAse activity. Following initial expression in yeast cells, the dimer component showed a tendency for nuclear localization. We thus fused a nuclear export signal (NES) LAEKLAGLDIN at its N terminus, which led to its cytosolic localization.

Plasmids and strains. The plasmids and strains resulting from this work are described in Supplementary Tables 2 and 3.

To achieve a stochastic expression of each component in yeast cells, each open reading frame (ORF) was inserted into a separate low-copy centromeric plasmid. The transfer RNA adaptation index of sequences for all components was optimized for *Saccharomyces cerevisiae*. Designed sequences were inserted into American Type Culture Collection yeast cassettes[52] using the polymerase incomplete primer extension cloning method[53]. For stoichiometric expression in Supplementary Video 1, sequences were inserted into M3925 plasmids[54] for genomic integration. Both components were cloned downstream of the yeast *TDH3* promoter. The selection markers for the dimer and tetramer were hygromycin and G418, respectively. Cloning was performed in *Escherichia coli* DH5α cells. Plasmids were subsequently isolated, verified by sequencing and transformed into either BY4741 (tetramer) or BY4742 (dimer) strains of S288C[55]. Expression in haploid cells was verified by microscopy and yeast were subsequently mated, creating diploid cells containing both plasmids. To investigate localization of mRNA, a modified version of the m-TAG method[27] was used. Rather than insertion of the MS2 loops into the 3′ untranslated region (UTR) using the Cre-Lox system, we utilized CRISPR–Cas9. We used the plasmid bRA89 (ref. [56]), which carries both the ORF for Cas9 and the guide RNA (gRNA). The gRNA was designed using CRISPR-ERA[57] to target the *TRP3* locus (GTGGACAATCTCACCAGCGT), and the dimer with the wild-type Im2, including the MS2 loops in its 3′ UTR, was inserted. For the insertion cassette, three pieces were amplified: one from the promoter to the stop codon, one from the stop codon to the end of the 3′ UTR containing 12 MS2 loop repeats and one from the end of the 3′ UTR to the end of the terminator. The primers for this amplification contained 40-bp homology regions to the *TRP3* locus on the flanking regions, and to each other in overlapping regions. The PCR products were treated with DPN1 (New England Biolabs) and purified using the Agencourt AMPure XP system. We transformed 20 µl of competent BY4742 cells with 1 µl (1 µg µl^{-1}) bRA89 (TRP3) and 200–300 ng of each module of the insertion cassette. After insertion of the dimer, cells were cotransformed with the plasmid carrying CP-3xGFP and a plasmid carrying the tetramer fused to mTagBFP2, rather than to Venus. For the negative control the insertion cassette consisted of three fragments: one with the *TDH3* promoter and GB1, one with the MS2L containing the 3′ UTR and one with the *CYC* terminator (refer to Supplementary Tables 1, 2 and 3 for details of proteins used in these constructs). The three fragments were purified with the Agencourt AMPure XP system, joined by PCR and the resulting piece was again purified. Five hundred nanograms of the product was cotransformed with 1 µg of bRA89 (TRP3) to 20 µl of competent BY4742 cells. The resulting strain was cotransformed with the CP-3xGFP plasmid, as well as with plasmids for the dimer and BFP-tagged tetramer. Finally, all strains were verified by sequencing. We note that, although one of the 12 MS2 loops was missing in the negative control, mRNAs were clearly visible in that strain, allowing unambiguous assessment of their colocalization with condensates.

Microscopy and image processing. Cells were imaged with an Olympus IX83 microscope coupled to a Yokogawa CSU-W1 spinning-disc confocal scanner with dual Hamamatsu ORCA-Flash4.0 V2 sCMOS cameras. Sixteen-bit images were acquired for brightfield and two confocal illumination schemes. For green fluorescence we used a 488 nm excitation (Ex) wavelength with a Toptica 100 mW laser and a bandpass emission (Em) filter (525/50 nm, Chroma ET/m). For red fluorescence we excited at 561 nm with an Obis 75 mW laser and used a bandpass emission filter (609/54 nm, Chroma ET/m). Imaging was performed with a ×60/1.35 numerical aperture (NA), oil-immersion objective (UPLSAPO60XO, Olympus), and FRAP experiments were carried out with a ×100/1.4 NA, oil-immersion objective (UPLSAPO100XO, Olympus). Automated imaging was performed with a motorized XY stage onto which a piezo-stage (Mad City Labs) was mounted and used for acquisition of *z*-stacks. For phase diagrams, we acquired seven *z*-stack images for each fluorescent channel and the average intensity projection was used. For time-lapse series, eight *z*-stacks were acquired and the maximum intensity projection was used.

Sample preparation for imaging. A liquid handling robot (Tecan Evo 200) was used to prepare Greiner 384-well glass-bottom optical imaging plates. For imaging, 0.5 µl of saturated cell suspension was transferred to an optical plate with synthetic defined (SD) medium and grown for 6 h to logarithmic growth. For time-lapse series, cells were grown to optical density $OD_{600} = 0.4–0.8$, transferred to matrical 96-well glass-bottom plates and covered with 0.5% agarose/SD medium containing the respective resistance marker. For time-lapse series of puromycin treatment, cells were not covered with agarose, but puromycin was added to the cells after 6 min of imaging to a final concentration of 10 mM. For treatment with puromycin and cycloheximide, a mixture of the drugs was added to yield a final concentration of 10 mM puromycin and 100 µg ml^{-1} cycloheximide. For FRAP experiments, cells were grown and left at saturation for 2 weeks to generate large condensates. Cells were subsequently fixed with ConA in an optical 96-well plate, as previously described[58], and FRAP experiments were carried out 6 h after their inoculation into fresh media.

Image analysis and generation of in vivo phase diagrams. Cells were identified, segmented and their fluorescent signal (median, average, minimum, maximum, tenth, twentieth, …, ninetieth percentile fluorescence) were identified, as well as additional cell properties, using custom algorithms[59] in ImageJ/FIJI[60], and exported as tabulated files. Condensates were identified in each cell independently, in a multistep process: (1) calculation of the median fluorescence intensity of pixels in a given cell; and (2) identification of the largest region composed of pixels with an intensity threefold above the median. If such a region existed and it showed circularity >0.4 and area >9 pixels, the cell was deemed to contain a condensate.

Tabulated data resulting from image analyses were loaded and analyzed with custom scripts in R. To convert fluorescent intensity to cytosolic concentration, His-tagged Venus and FusionRed were purified using the GE Healthcare His GraviTrap system. Serial dilutions of each protein were generated, fluorescence intensities were recorded and a linear model was fitted (Supplementary Fig. 1). A fluorescent plastic slide (Chroma Technology) served as a constant reference to calibrate fluorescence signals of experiments carried out on different days. Fluorescence signals of the experiments were normalized according to the fluorescent slide, and cytosolic concentrations were inferred from regression of purified proteins. Finally, cells with condensates were excluded and the median cytosolic concentrations of YFP and RFP were plotted against each other.

FRAP. A macro created in VisiView v.4.4 software was written to capture images on the red channel in rapid succession during the course of a FRAP experiment. Photobleaching was achieved with a 405-nm laser pulse lasting 20 ms after the tenth frame of the acquired series. The RFP channel exposure was set to 50 ms. Images were acquired every 100 ms. We acquired 250 frames for a total acquisition time of 25 s.

Lattice model of dimers and tetramers. The tetramer–dimer attraction is the only interaction energy in this simplified lattice model. Nearest-neighbor tetramers or dimers separated by solvent molecules do not interact. Higher-order neighbor interactions are rejected and the zero of energy is set by the tetramer– and dimer–solvent interactions, which we take to be equal for simplicity. The thermodynamic criteria required for coexistence are equal chemical potential and osmotic pressure for each species (tetramer, dimer and solvent molecules) in the two phases. The model captures these effects to predict the concentration, temperature and binding strength regimes where phase separation occurs. A mean-field theory and calculation resuling in the phase diagrams shown in the main text are described in ref. [61].

The experimental data corresponding to the interaction 1.5×10^{-8} M are about $18\,k_BT$, where k_B is the Boltzmann constant and T the temperature. (Fig. 2g). The lattice model involves solving four nonlinear algebraic equations to find the equilibrium concentrations of the complexes, and then using interpolation we determine the analytical expression for the free energy that we finally use to find the binodal phase diagram numerically. This procedure makes it hard numerically to find the binodal for very large interaction strengths. The theory shows that the minima of phase diagrams vary exponentially with interaction strength[61]. For these reasons, we show an overlay of the theoretical binodal (and not a fit) on the experimental data.

FRAP data analysis. Custom macros were created in ImageJ/FIJI[60] to extract quantitative data from the image series. Data were first extracted from both bleached and nonbleached areas by manual selection of two pixel coordinates, the first at the center of the bleached region and second at the center of the nonbleached region. A circular region of interest (ROI) of six pixels in diameter was

then generated. Because small movements of the condensate may have occurred when recording the video, we generated 42 additional adjacent ROIs by translation of either 0.5, 1.0, 1.5 or 2.0 pixels in all directions, generating 6, 8, 12 or 16 ROIs for each distance, respectively. The average intensity of each ROI was then extracted for every frame of the image series. ROI intensities were subsequently analyzed with custom scripts in R. First, for each of the two locations (bleached and unbleached), we averaged five sub-ROIs showing either the lowest (bleached area) or highest total fluorescence intensity (nonbleached area). For each frame, the intensity recorded for the bleached area was divided by the intensity of the nonbleached area. Finally, the values were normalized as follows: $x_{\mathrm{norm}} = \frac{x - x_{\mathrm{min}}}{\max(x - x_{\mathrm{min}})}$, where x is the ratio of integrated pixel intensities measured for bleached/unbleached ROI and x_{min} is the minimum value of x across the image series.

Reporting Summary. Further information on research design is available in the Nature Research Reporting Summary linked to this article.

Data availability

We provide single-cell measurements of YFP and RFP concentrations for all phase diagrams in two Supplementary Excel tables. Other data are available from the authors upon request. Source Data are provided with this paper.

Code availability

Code and custom scripts used in this work are available from the authors upon request. We used the open source package oxDNA (v.2.4) to run the sedimentation simulations.

References

52. Mumberg, D., Müller, R. & Funk, M. Yeast vectors for the controlled expression of heterologous proteins in different genetic backgrounds. *Gene* **156**, 119–122 (1995).
53. Klock, H. E. & Lesley, S. A. The Polymerase Incomplete Primer Extension (PIPE) method applied to high-throughput cloning and site-directed mutagenesis. *Methods Mol. Biol.* **498**, 91–103 (2009).
54. Voth, W. P., Jiang, Y. W. & Stillman, D. J. New 'marker swap' plasmids for converting selectable markers on budding yeast gene disruptions and plasmids. *Yeast* **20**, 985–993 (2003).
55. Brachmann, C. B. et al. Designer deletion strains derived from *Saccharomyces cerevisiae* S288C: a useful set of strains and plasmids for PCR-mediated gene disruption and other applications. *Yeast* **14**, 115–132 (1998).
56. Anand, R., Beach, A., Li, K. & Haber, J. Rad51-mediated double-strand break repair and mismatch correction of divergent substrates. *Nature* **544**, 377–380 (2017).
57. Liu, H. et al. CRISPR–ERA: a comprehensive design tool for CRISPR-mediated gene editing, repression and activation. *Bioinformatics* **31**, 3676–3678 (2015).
58. Cohen, Y. & Schuldiner, M. Advanced methods for high-throughput microscopy screening of genetically modified yeast libraries. *Methods Mol. Biol.* **781**, 127–159 (2011).
59. Matalon, O., Steinberg, A., Sass, E., Hausser, J. & Levy, E. D. Reprogramming protein abundance fluctuations in single cells by degradation. Preprint at *bioRxiv* https://doi.org/10.1101/260695 (2018).
60. Schindelin, J. et al. Fiji: an open-source platform for biological-image analysis. *Nat. Methods* **9**, 676–682 (2012).
61. Nandi, S. K., Heidenreich, M., Levy, E. D. & Safran, S. A. Interacting multivalent molecules: affinity and valence impact the extent and symmetry of phase separation. Preprint at https://arxiv.org/abs/1910.11193 (2019).

Acknowledgements

We thank J. Gerst and R. R. Nair (Weizmann Institute) for sharing plasmids of the MS2 system, S. Schwartz (Weizmann Institute) for the bRA89 plasmid, F. Sciortino and H. Hofmann for helpful discussions and suggestions and H. Greenblatt for help with computer systems. E.D.L. acknowledges support by the Israel Science Foundation (no. 1452/18), by the European Research Council under the European Union's Horizon 2020 research and innovation program (grant agreement no. 819318), by the HFSP Career Development Award (award no. CDA00077/2015), by a research grant from A.-M. Boucher and by research grants from the Estelle Funk Foundation, the Estate of Fannie Sherr, the Estate of Albert Delighter, the Merle S. Cahn Foundation, Mrs. Mildred S. Gosden, the Estate of Elizabeth Wachsman and the Arnold Bortman Family Foundation. E.D.L. is an incumbent of the Recanati Career Development Chair of Cancer Research. L.R. acknowledges support from the European Commission (Marie Skłodowska-Curie Fellowship, no. 702298-DELTAS). S.A.S. thanks the BSF and the ISF program and acknowledges the historical generosity of the Perlmann family foundation. S.K.N. acknowledges support from the Koshland foundation and Department of Atomic Energy (DAE), India. E.L. and L.R. thank the Vienna Scientific Cluster (VSC) for computing time.

Author contributions

M.H., J.M.G. and E.D.L. designed the research and synthetic protein system. M.H. and J.M.G. performed the experiments with help from Y.N. E.L., L.R. and J.K.P.D developed the theoretical framework for modeling the system based on patchy particles. S.K.N. and S.A.S. developed the theoretical framework for modeling the system based on a lattice model. A.S. wrote the image analysis scripts. E.S. carried out electron microscopy experiments. M.H. and E.D.L. wrote the manuscript with input from all authors.

Competing interests

The authors declare no competing interests.

Additional information

Extended data is available for this paper at https://doi.org/10.1038/s41589-020-0576-z.

Supplementary information is available for this paper at https://doi.org/10.1038/s41589-020-0576-z.

Correspondence and requests for materials should be addressed to L.R., S.A.S., J.P.K.D. or E.D.L.

Reprints and permissions information is available at www.nature.com/reprints.

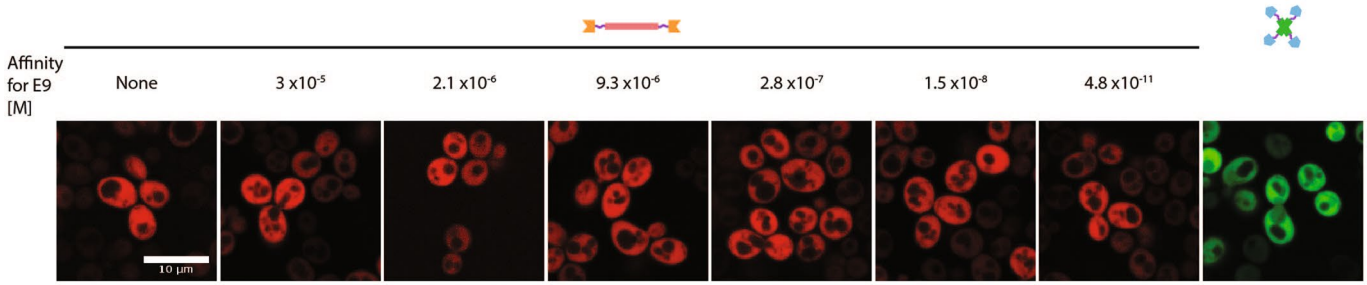

Extended Data Fig. 1 | The components do not form condensates when expressed individually. Haploid cells expressing only one of the building blocks show a homogenous distribution of fluorescence throughout the cytoplasm. The left-most image shows cells expressing the dimer component lacking the Im2 domain. The next images show cells expressing the variants of the dimer component in the absence of the tetramer component. The right-most image shows cells expressing the tetramer component in the absence of the dimer component. This result was replicated three times.

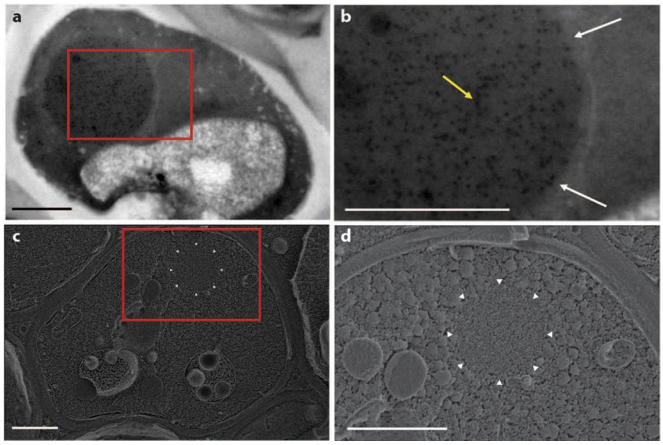

Extended Data Fig. 2 | The synthetic condensates are not membrane-bound. a, Transmission electron microscopy (TEM) micrograph of fixed and sectioned yeast shows a condensate formed by our minimal system, in the cytoplasm. **b**, The yellow arrow points to one of several 10 nm gold-labeled anti-GFP antibodies, confirming the identity of the designed compartments. White arrows highlight the lack of membrane surrounding the compartment. **c**, Scanning electron microscopy micrograph of cells frozen at high-pressure and cryo-fractured reveals the mosaic of amorphic cytoplasm. The region outlined by white carets exhibits a distinct ultrastructure **d**, Increased magnification of a suspected condensate within the cytoplasm, outlined with white carets. This ultrastructure has no visible membrane. Scale bar 1 μm. We did not carry independent biological replicates of these electron microscopy experiments.

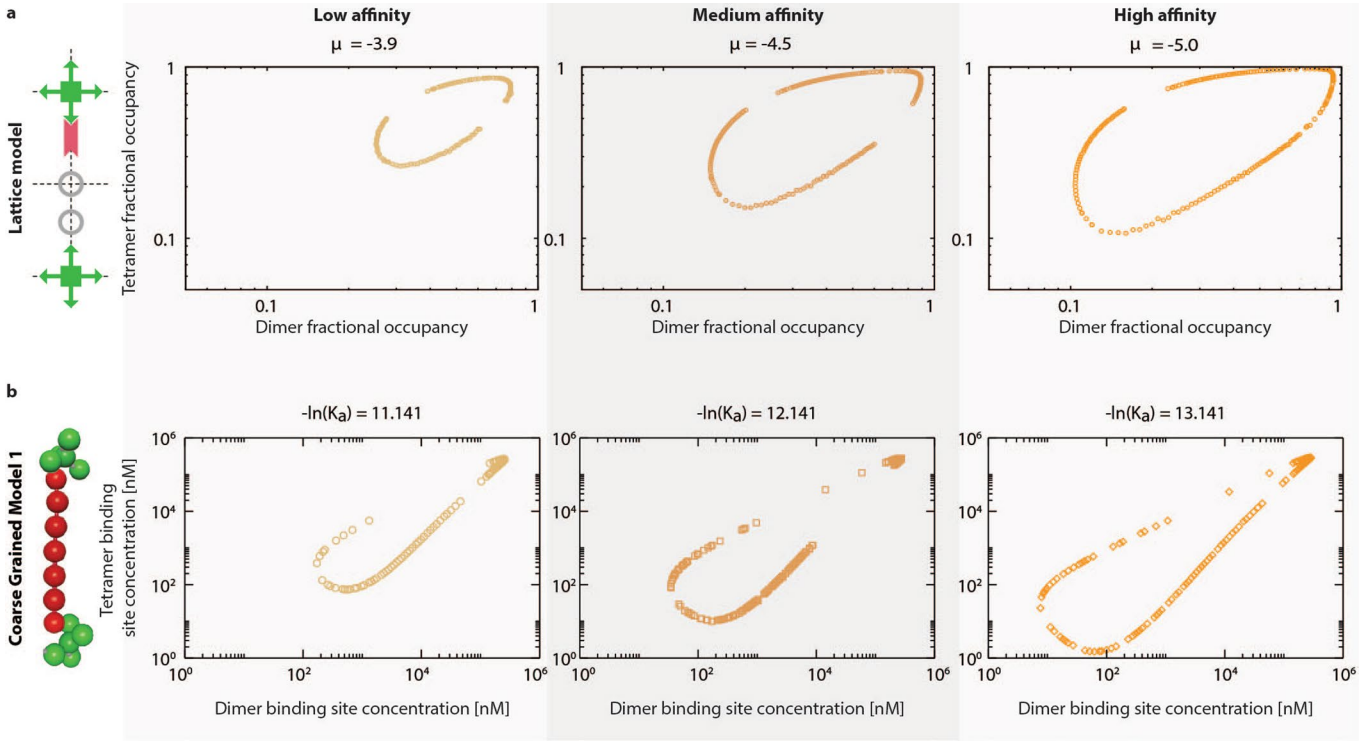

Extended Data Fig. 3 | Impact of affinity on the phase diagram of the dimer-tetramer system. a, We used a lattice model (Supplementary Note, Section 1) of the dimer-tetramer system. In the square lattice, concentration is measured by fractional occupancy of edges and vertices by dimers and tetramers respectively. We calculated the binodal of this system in the plane corresponding to the fractional occupancy of dimer (x-axis) and tetramer (y-axis). Affinity increases in panels from left to right, where μ is the binding energy in units of kT of a linker and one arm of the tetravalent molecule. Higher affinity (larger μ) increases the fraction of the phase-separated region. **b**, We used mean-field theoretical calculations of patchy particles matching the geometry of the proteins. The binodal is calculated in the plane corresponding to the concentration of dimers (x-axis) and tetramers (y-axis). Affinity (which is linked to the energy and entropy associated with the formation of a bond, see Supplementary Note, Section 1) increases from left to right.

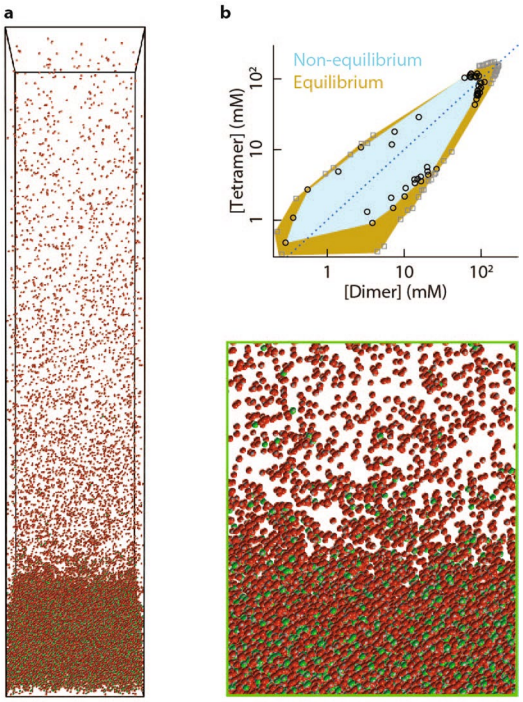

Extended Data Fig. 4 | Simulations recapitulate the kinetic trapping effect observed experimentally. a, Sedimentation molecular dynamics simulation of patchy particles. Several simulations were conducted at equilibrium or out-of-equilibrium while sampling different concentrations of dimer and tetramer. The protein osmotic pressure as a function of density was inferred from each simulation and used to evaluate the phase boundaries. **b**, The phase diagram of the patchy mixture computed with equilibrium and non-equilibrium simulations (squares and circles, respectively).

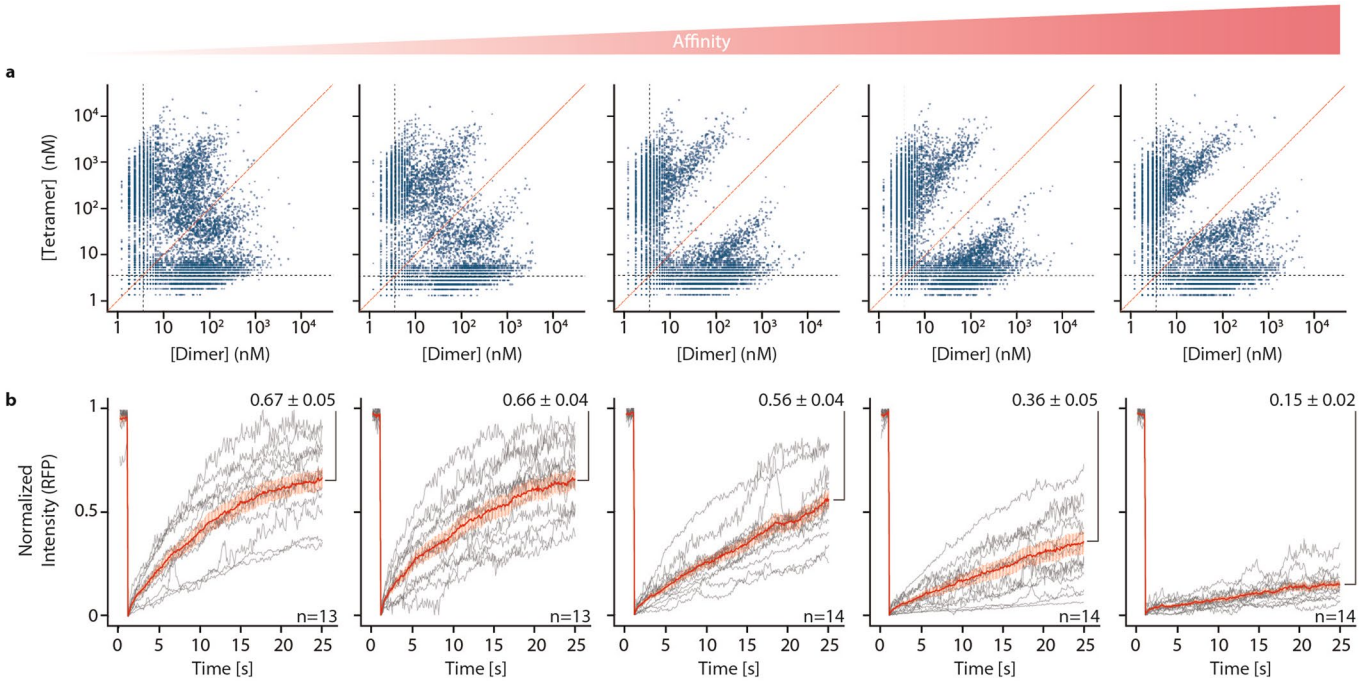

Extended Data Fig. 5 | *In vivo* phase diagrams and fluorescence recovery profiles observed with different affinities. a, *In vivo* phase diagrams observed for five affinities investigated initially. Concentrations correspond to those of the binding sites (not of the dimer and tetramer complexes). The red line highlights the diagonal, where the concentrations of binding sites of dimer and tetramers are equal. The grey dotted lines show the lower limit of concentrations that can be reliably estimated. **b**, Fluorescence recovery profiles of photobleached condensates for different interaction affinities between the components. Grey lines show individual experiments, the red line corresponds to the mean recovery and the transparent red area indicates the standard error. The mean recovery after 25 seconds and associated standard error are given for each affinity.

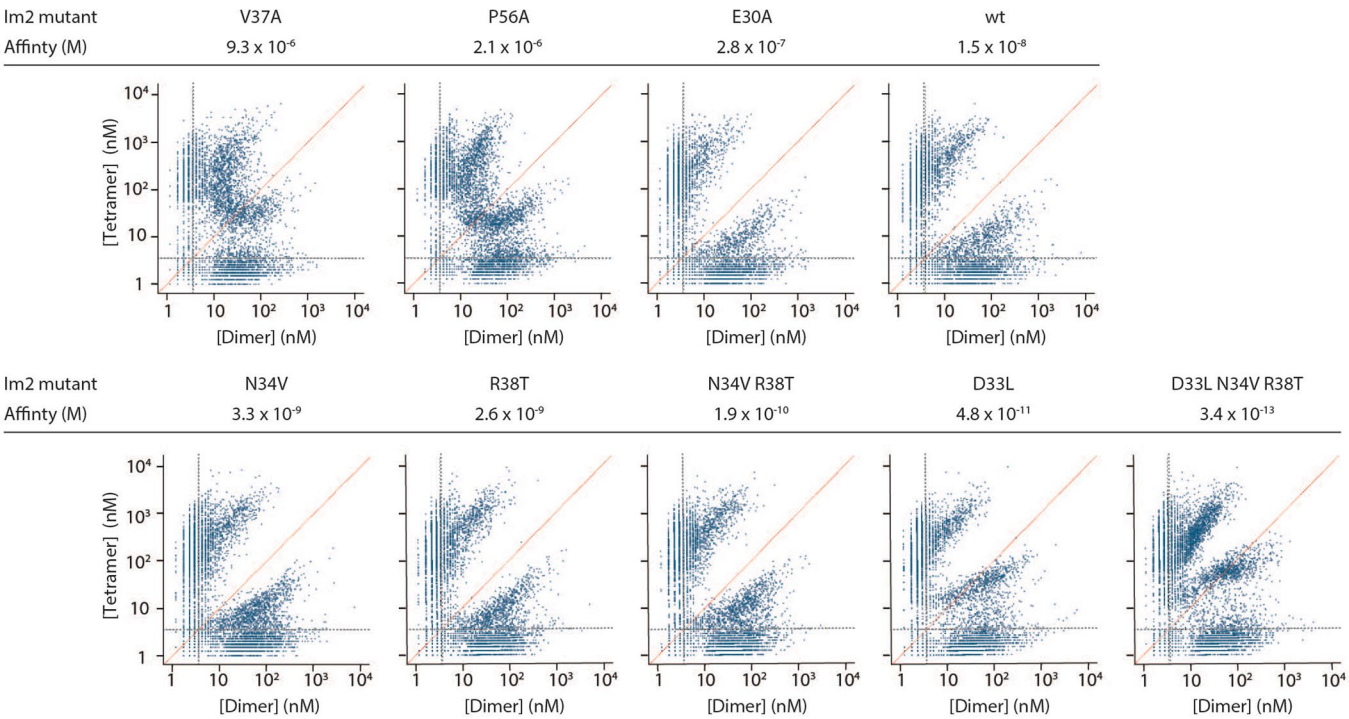

Extended Data Fig. 6 | Replicating the measurement of *in vivo* phase diagrams with four additional affinities. Phase diagrams measured for nine affinities. Five affinities come from replicating experiments shown in Extended Data Fig. 5, and four are new. Concentrations correspond to those of the binding sites (not of the dimer and tetramer complexes). The red line highlights the diagonal, where the concentrations of binding sites of dimer and tetramers are equal. The grey dotted lines show the lower limit of concentrations that can be reliably estimated. Affinities and mutations are indicated above. The N34V, R38T, double N34V/R38T and triple D33L/N34V/R38T mutants were added later to further investigate the out-of-equilibrium effect. The same number of randomly selected cells were plotted in all panels (n=4000) to allow comparing the density of points across plots.

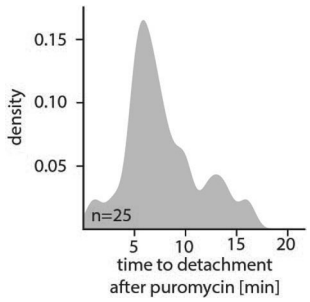

Extended Data Fig. 7 | The mRNA coding for the dimer is released from condensates within minutes after the addition of puromycin. Cells were treated with a final concentration of 10 mM puromycin and mRNA release from the condensate was followed by time-lapse microscopy.

nature research

Corresponding author(s): Emmanuel Levy

Last updated by author(s): May 6, 2020

Reporting Summary

Nature Research wishes to improve the reproducibility of the work that we publish. This form provides structure for consistency and transparency in reporting. For further information on Nature Research policies, see Authors & Referees and the Editorial Policy Checklist.

Statistics

For all statistical analyses, confirm that the following items are present in the figure legend, table legend, main text, or Methods section.

n/a	Confirmed	
☐	☒	The exact sample size (*n*) for each experimental group/condition, given as a discrete number and unit of measurement
☐	☒	A statement on whether measurements were taken from distinct samples or whether the same sample was measured repeatedly
☐	☒	The statistical test(s) used AND whether they are one- or two-sided *Only common tests should be described solely by name; describe more complex techniques in the Methods section.*
☒	☐	A description of all covariates tested
☒	☐	A description of any assumptions or corrections, such as tests of normality and adjustment for multiple comparisons
☐	☒	A full description of the statistical parameters including central tendency (e.g. means) or other basic estimates (e.g. regression coefficient) AND variation (e.g. standard deviation) or associated estimates of uncertainty (e.g. confidence intervals)
☐	☒	For null hypothesis testing, the test statistic (e.g. *F*, *t*, *r*) with confidence intervals, effect sizes, degrees of freedom and *P* value noted *Give P values as exact values whenever suitable.*
☒	☐	For Bayesian analysis, information on the choice of priors and Markov chain Monte Carlo settings
☒	☐	For hierarchical and complex designs, identification of the appropriate level for tests and full reporting of outcomes
☐	☒	Estimates of effect sizes (e.g. Cohen's *d*, Pearson's *r*), indicating how they were calculated

Our web collection on statistics for biologists contains articles on many of the points above.

Software and code

Policy information about availability of computer code

Data collection	For aquisition of microscopy images, VisiView Version 4.4 was used.
Data analysis	For image analysis, we used custom FIJI/imageJ and R scripts. A detailed description can be found at doi: https://doi.org/10.1101/260695 . For generating in vivo phase diagrams and analyzing FRAP experiments, custom R and FIJI/ImageJ scripts were used. Molecular dynamics simulations were carried out with the oxdna package (v2.4) (https://sourceforge.net/projects/oxdna). Coexistence curves were derived from thermodynamical calculations based on custom python and C scripts. Scripts are available from the authors upon request.

For manuscripts utilizing custom algorithms or software that are central to the research but not yet described in published literature, software must be made available to editors/reviewers. We strongly encourage code deposition in a community repository (e.g. GitHub). See the Nature Research guidelines for submitting code & software for further information.

Data

Policy information about availability of data

All manuscripts must include a data availability statement. This statement should provide the following information, where applicable:

- Accession codes, unique identifiers, or web links for publicly available datasets
- A list of figures that have associated raw data
- A description of any restrictions on data availability

The raw data for the phase diagrams is provided in Excel files. Other data can be obtained from the authors upon request.

Field-specific reporting

Please select the one below that is the best fit for your research. If you are not sure, read the appropriate sections before making your selection.

☒ Life sciences ☐ Behavioural & social sciences ☐ Ecological, evolutionary & environmental sciences

For a reference copy of the document with all sections, see nature.com/documents/nr-reporting-summary-flat.pdf

Life sciences study design

All studies must disclose on these points even when the disclosure is negative.

Sample size	For phase diagrams, enough images (typically containing thousands of cells) were collected to allow the visual identification of phase boundaries. For FRAP, 13 or 14 independent condensates were targeted to yield a low standard error of the average recovery profile. For molecular dynamics simulations, we used a box size such that finite size effects do not alter appreciably our results.
Data exclusions	Only pre-established criteria were used, for example we excluded cells without condensates for the phase diagrams.
Replication	Replication statements appear with each corresponding figure. Electron microscopy work was not replicated, only one attempt was made, of which the results are shown
Randomization	Cells were chosen randomly or selected according to objective criteria, as described
Blinding	For phase diagrams, blinding is not relevant, because the microscope takes pictures of random fields of view. For FRAP data and molecular dynamics simulations, no blinding was used.

Reporting for specific materials, systems and methods

We require information from authors about some types of materials, experimental systems and methods used in many studies. Here, indicate whether each material, system or method listed is relevant to your study. If you are not sure if a list item applies to your research, read the appropriate section before selecting a response.

Materials & experimental systems

n/a	Involved in the study
☒	☐ Antibodies
☐	☒ Eukaryotic cell lines
☒	☐ Palaeontology
☒	☐ Animals and other organisms
☒	☐ Human research participants
☒	☐ Clinical data

Methods

n/a	Involved in the study
☒	☐ ChIP-seq
☒	☐ Flow cytometry
☒	☐ MRI-based neuroimaging

Eukaryotic cell lines

Policy information about cell lines

Cell line source(s)	The original yeast strains used were obtained from another lab (Maya Schuldiner)
Authentication	Auxotrophies were as expected
Mycoplasma contamination	NA
Commonly misidentified lines (See ICLAC register)	NA